



Cite this: *RSC Adv.*, 2019, 9, 4682

# Effect of initial support particle size of MnO<sub>x</sub>/TiO<sub>2</sub> catalysts in the selective catalytic reduction of NO with NH<sub>3</sub>†

Yang Yang,<sup>ab</sup> Zhun Hu,<sup>id</sup>\*<sup>a</sup> Rongli Mi,<sup>a</sup> Dan Li,<sup>a</sup> Xiang Yong,<sup>a</sup> Huie Yang<sup>b</sup> and Kunfeng Liu<sup>b</sup>

A series of manganese-based catalysts supported by 5–10 nm, 10–25 nm, 40 nm and 60 nm anatase TiO<sub>2</sub> particles was synthesized *via* an impregnation method to investigate the effect of the initial support particle size on the selective catalytic reduction (SCR) of NO with NH<sub>3</sub>. All catalysts were characterized by transmission electron microscopy (TEM), N<sub>2</sub> physisorption/desorption, X-ray diffraction (XRD), temperature programmed techniques, X-ray photoelectron spectroscopy (XPS) and *in situ* diffuse reflectance infrared transform spectroscopy (DRIFTS). TEM results indicated that the particle sizes of the MnO<sub>x</sub>/TiO<sub>2</sub> catalysts were similar after the calcination process, although the initial TiO<sub>2</sub> support particle sizes were different. However, the initial TiO<sub>2</sub> support particle sizes were found to have a significant influence on the SCR catalytic performance. XPS and NH<sub>3</sub>-TPD results of the MnO<sub>x</sub>/TiO<sub>2</sub> catalysts illustrated that the surface Mn<sup>4+</sup>/Mn molar ratio and acid amount could be influenced by the initial TiO<sub>2</sub> support particle sizes. The order of surface Mn<sup>4+</sup>/Mn molar ratio and acid amount over the MnO<sub>x</sub>/TiO<sub>2</sub> catalysts was as follows: MnO<sub>x</sub>/TiO<sub>2</sub>(10–25) > MnO<sub>x</sub>/TiO<sub>2</sub>(40) > MnO<sub>x</sub>/TiO<sub>2</sub>(60) > MnO<sub>x</sub>/TiO<sub>2</sub>(5–10), which agreed well with the order of SCR performance. *In situ* DRIFTS results revealed that the NH<sub>3</sub>-SCR reactions over MnO<sub>x</sub>/TiO<sub>2</sub> at low temperature occurred *via* a Langmuir–Hinshelwood mechanism. More importantly, it was found that the bridge and bidentate nitrates were the main active substances for the low-temperature SCR reaction, and bridge nitrate adsorbed on Mn<sup>4+</sup> showed superior SCR activity among all the adsorbed NO<sub>x</sub> species. The variation of the initial TiO<sub>2</sub> support particle size over MnO<sub>x</sub>/TiO<sub>2</sub> could change the surface Mn<sup>4+</sup>/Mn molar ratio, which could influence the adsorption of NO<sub>x</sub> species, thus bringing about the diversity of the SCR catalytic performance.

Received 7th December 2018  
 Accepted 19th January 2019

DOI: 10.1039/c8ra10077b

[rsc.li/rsc-advances](http://rsc.li/rsc-advances)

## 1 Introduction

Nitrogen oxides (NO<sub>x</sub>), as a harmful exhaust emission, can induce various human health and environmental hazards, such as acid rain, photochemical smog, and ozone layer depletion.<sup>1,2</sup> Increasing attention has been focused on NO<sub>x</sub> abatement, including NO<sub>x</sub> storage-reduction (NSR or LNT),<sup>3–5</sup> NO<sub>x</sub> decomposition, and Selective Catalytic Reduction (SCR).<sup>6–8</sup> SCR technology has been regarded as the most promising way to remove NO<sub>x</sub>, and has been commercially applied in diesel engines and power plants. However, due to increasingly strict emission legislation, it is crucial to develop

future catalysts for low-temperature NO<sub>x</sub> abatement techniques, to meet future exhaust gas emission legislation.<sup>9</sup>

Because of their various valence states and low cost, transition metal oxides (MnO<sub>x</sub>, FeO<sub>x</sub>, CoO<sub>x</sub>, CuO<sub>x</sub>), are usually used as catalysts in SCR research.<sup>6–18</sup> Owing to their inherent instability and poor anti-sintering ability, transition metal oxides are usually supported on an “inert” support to enhance their thermal stability and catalyst lifespan. Pena *et al.*<sup>19</sup> investigated low-temperature SCR using VO<sub>x</sub>, CrO<sub>x</sub>, MnO<sub>x</sub>, FeO<sub>x</sub>, CoO<sub>x</sub>, NiO<sub>x</sub> and CuO<sub>x</sub> catalysts supported on TiO<sub>2</sub>. The SCR activity for the various transition metal oxides as active sites supported on TiO<sub>x</sub> decreased in the following order: MnO<sub>x</sub> > CuO<sub>x</sub> ≥ CrO<sub>x</sub> ≥ CoO<sub>x</sub> > FeO<sub>x</sub> ≫ VO<sub>x</sub> ≫ NiO<sub>x</sub>, indicating that MnO<sub>x</sub> was the most promising catalyst for future practical applications. Among supported catalysts, the properties of the support and the interaction between MnO<sub>x</sub> and the support are often considered to be the main parameters affecting the catalytic activity. Smirniotis *et al.*<sup>20</sup> synthesized a series of manganese oxides supported on TiO<sub>2</sub>, Al<sub>2</sub>O<sub>3</sub>, and SiO<sub>2</sub> to investigate the influence of the support on SCR activity with a space velocity 8000 h<sup>-1</sup>. They found that the SCR activity of the supported MnO<sub>x</sub>

<sup>a</sup>Institute of Industrial Catalysis, School of Chemical Engineering and Technology, Xi'an Jiaotong University, Xi'an, Shaanxi 710049, China. E-mail: huzhun@mail.xjtu.edu.cn; Fax: +86-29-82663189; Tel: +86-29-82663189

<sup>b</sup>Sinochem Modern Environmental Protection Chemicals (Xi'an) Co. LTD., Xi'an, Shaanxi 710201, China

† Electronic supplementary information (ESI) available. See DOI: 10.1039/c8ra10077b



catalysts decreased in the following order: TiO<sub>2</sub> (anatase) > SiO<sub>2</sub> > TiO<sub>2</sub> (rutile) > TiO<sub>2</sub> (anatase, rutile) >  $\gamma$ -Al<sub>2</sub>O<sub>3</sub>. MnO<sub>x</sub>/TiO<sub>2</sub> (anatase) showed excellent NO<sub>x</sub> abatement activity, even at 120 °C when it reached complete conversion. Therefore, MnO<sub>x</sub>/TiO<sub>2</sub> catalysts have been investigated on the basis of the effects of the preparation method,<sup>21</sup> manganese precursors<sup>22</sup> and manganese loading<sup>23</sup> on SCR activity.<sup>19,24</sup> However, the interaction between manganese oxides and TiO<sub>2</sub> has not been fully investigated, especially on the effect of the support size.

The interaction between the active component and the support is not only influenced by the support type, but also relies on the size of the support.<sup>25–30</sup> Soykal *et al.*<sup>30</sup> studied the effect of support particle size in steam reforming of ethanol over CoO<sub>x</sub>/CeO<sub>2</sub> catalysts with CeO<sub>2</sub> support particle sizes in the micro- and nano-range. CoO<sub>x</sub>/CeO<sub>x</sub> with smaller CeO<sub>2</sub> particle sizes manifested superior catalytic performance and coking resistance ability. These results can be ascribed to a combination of factors, including reducibility, dispersion and redox sites on the catalyst surface. All of these properties could be affected by the particle size of the support, thus leading to different catalytic performances. Pakulska *et al.*<sup>28</sup> investigated the effect of support particle size over NiO/ZrO<sub>2</sub> and NiO/CeO<sub>2</sub> on the catalytic oxidation of methane. They found that zirconia particles size could change the number of catalytic sites *via* varying the pre-exponential factor and ceria size could change the reaction activation energy by varying oxygen transport to the active sites. Xu *et al.*<sup>25–27</sup> studied a series of Ni/ZrO<sub>2</sub> catalysts with various ZrO<sub>2</sub> particle sizes to systematically investigate the effect of support particle size on the reforming of methane with CO<sub>2</sub>. Their proposed nanocomposite catalyst, which could be defined as a catalyst with comparable Ni metal and zirconia nanocrystals, showed superior catalytic activity and long-term stability. They attributed this excellent catalytic performance to the boundary or perimeter between Ni and ZrO<sub>2</sub>, which could easily be generated by similar-sized Ni and ZrO<sub>2</sub> particles. All of the above examples illustrate that the support size can significantly influence the catalytic performance and catalyst lifespan, by affecting the properties of active sites or the boundary between active sites and the support. However, up until now, corresponding research regarding the effect of support size on NO<sub>x</sub> abatement has rarely been reported.

In this work, a series of MnO<sub>x</sub>/TiO<sub>2</sub> catalysts was prepared *via* an impregnation method with a variation of TiO<sub>2</sub> support particle sizes to investigate the effect of the initial TiO<sub>2</sub> support size on the SCR performance. In addition, these catalysts were characterized by N<sub>2</sub> physisorption, TEM, XRD, H<sub>2</sub>-TPR, O<sub>2</sub>-TPD, XPS and DRIFTS, to understand the effects of the structure, redox properties and active site-support interaction on the SCR catalysis.

## 2 Experimental

### 2.1 Preparation of catalysts

Anatase TiO<sub>2</sub> particles of various sizes (Aladdin Reagent Co., Ltd.) were used as support materials without any purification. All of the catalysts were synthesized *via* a wet impregnation method. In a typical process, 2 g TiO<sub>2</sub> with various particle sizes

and 0.84 mL 50 wt% Mn(NO<sub>3</sub>)<sub>2</sub> (Tianjin Fuchen chemical reagents company) were added into 20 mL deionized water, and the mixture was vigorously stirred for 24 h at room temperature. Then the solution was dried under vacuum at 60 °C in a rotary evaporator. The obtained powder was dried at 110 °C overnight, and then calcined at 550 °C for 5 h with a heating rate of 1 °C min<sup>-1</sup> in a muffle furnace. The obtained materials were denoted as MnO<sub>x</sub>/TiO<sub>2</sub>(*n*), where *n* represents the particle size of TiO<sub>2</sub>. The actual manganese loading of the catalysts was determined by X-ray fluorescence spectrometry (XRF).

### 2.2 Catalytic test

A catalytic performance test for the NH<sub>3</sub>-SCR reaction was implemented in a fixed-bed plug-flow stainless-steel tubular reactor (*L* = 60 cm,  $\Phi_{in}$  = 7 mm). The typical components of the simulated gas were as follows: 500 ppm NO, 500 ppm NH<sub>3</sub>, 5 vol% O<sub>2</sub> and balance Ar with a space velocity of 40 000 mL g<sup>-1</sup> h<sup>-1</sup>. The reaction temperature was recorded by a K-type thermocouple located inside the tube near the catalyst bed. Prior to the SCR catalytic measurements, the catalyst was pretreated in 20 vol% O<sub>2</sub>/Ar at 400 °C for 1 h. The reaction was carried out from 50 °C to 350 °C with an increment of 25 °C and each temperature was held for 1 h to obtain a stable reaction conversion. The concentration of NO<sub>x</sub> was detected by a fuel analyzer (AFRISO, M 60). NO<sub>x</sub> conversion was calculated using the following equation:

$$\text{NO}_x \text{ conversion (\%)} = \frac{[\text{NO}_x]_{in} - [\text{NO}_x]_{out}}{[\text{NO}_x]_{in}} \times 100$$

### 2.3 Catalyst characterization

N<sub>2</sub> adsorption–desorption isotherms were collected at –196 °C on a BELSORP-Max analyzer. Prior to each measurement, the catalyst was degassed under high vacuum at 300 °C for 3 h. The surface area of each sample was obtained using the Brunauer–Emmett–Teller (BET) method and the pore size distribution was determined *via* the Barrett–Joyner–Halenda (BJH) method using desorption branch.

X-ray diffraction (XRD) patterns were measured on a SHIMADZU XRD-6100 Powder diffractometer using a Cu K $\alpha$  radiation source ( $\lambda$  = 0.15406 nm). The diffraction patterns were recorded over a  $2\theta$  range of 10–80° with a scan speed of 6 ° min<sup>-1</sup> and a step size of 0.02°.

H<sub>2</sub>-temperature programmed reduction (H<sub>2</sub>-TPR) experiments were performed on a Quantachrome ChemBET Pulsar chemisorption analyzer with a thermal conductivity detector (TCD). H<sub>2</sub>-TPR curves were acquired in 5 vol% H<sub>2</sub>/He from 50 °C to 800 °C with a temperature rate of 10 °C min<sup>-1</sup> and held at 800 °C for 30 min. Prior to each measurement, about 0.040 g sample was pretreated from room temperature to 500 °C with a temperature rate of 10 °C min<sup>-1</sup> in a flowing purified He gas (30 mL min<sup>-1</sup>) and was then kept at 500 °C for 30 min, in order to remove weakly adsorbed moisture and gas on the catalyst surface. After the sample was cooled to 50 °C, the flowing gas was switched to 5 vol% H<sub>2</sub> + He (30 mL min<sup>-1</sup>) and the sample



was purged for 30 min until the TCD signal was stable. NH<sub>3</sub>-temperature programmed desorption (NH<sub>3</sub>-TPD) experiments were carried out using the same equipment. NH<sub>3</sub>-TPD curves were obtained in flowing He (30 mL min<sup>-1</sup>) from 50 °C to 800 °C with a temperature ramp rate of 10 °C min<sup>-1</sup>, and 800 °C was held for 30 min. The pretreatment procedure for NH<sub>3</sub>-TPD was similar to that of H<sub>2</sub>-TPR. Adsorption of NH<sub>3</sub> was conducted under flowing 5 vol% NH<sub>3</sub> + He for *ca.* 30 min at 100 °C, and then purged with flowing He until the baseline became stable.

O<sub>2</sub>-TPD experiments were performed on a mass spectrometer (TILON GRP TECHNOLOGY LIMITED LC-D200M). O<sub>2</sub>-TPD curves were obtained under flowing N<sub>2</sub> (30 mL min<sup>-1</sup>) from 100 °C to 800 °C with a temperature ramp rate of 10 °C min<sup>-1</sup>, and 800 °C was held for 30 min. Prior to each measurement, about 100 mg of sample was pretreated in a U-shaped quartz tube at 500 °C for 30 min under flowing N<sub>2</sub> (30 mL min<sup>-1</sup>), followed by cooling to 100 °C. Adsorption of oxygen was then conducted at 20 vol% O<sub>2</sub> + N<sub>2</sub> for *ca.* 30 min at 100 °C until the O<sub>2</sub> signal became stable. After purging with flowing N<sub>2</sub> until the baseline signal reached a stable state, the O<sub>2</sub>-TPD signals began to be recorded with the mass-to-charge ratios (*m/z* = 16 and 32).

Transmission Electron Microcopy (TEM) was conducted on a Tecnai G2 F20 transmission electron microscope. More than 200 particles were randomly measured to determine the mean diameter of TiO<sub>2</sub> and MnO<sub>x</sub>/TiO<sub>2</sub> catalysts, using the equation  $d = \sum(n_i d_i) / \sum n_i$ , where *n<sub>i</sub>* is the number of particles with a diameter of *d<sub>i</sub>*.

The components of the catalysts were examined on a Bruker S8 TIGERX X-Ray Fluorescence analyzer (XRF), equipped with a 60 kV X-ray tube (Rh K $\alpha$  radiation) with a maximum power of 4 W, and a maximum current of 170 mA. The XPS spectra were conducted on a Kratos Analytical AXIS Ultra DLD spectrometer with an Al K $\alpha$  radiation source (*h* $\nu$  = 1253.6 eV), operated at an accelerating power of 15 kW. The samples were degassed with vacuum-pumping to 5  $\times$  10<sup>-7</sup> Pa before the measurement. The binding energy was calibrated by the C 1s peak at 284.8 eV and the final spectra were obtained by subtracting a Shirley-type background.

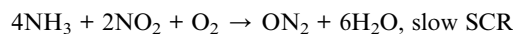
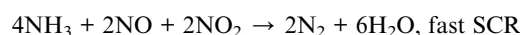
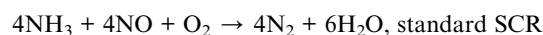
*In situ* diffusion reflection infrared Fourier transformed spectroscopy (DRIFTS) experiments were conducted on a Nicolet iS50 FTIR spectrometer equipped with a DRIFT cell containing ZnSe windows and MCT detector.<sup>31</sup> The spectra were obtained from 4000 to 525 cm<sup>-1</sup> at a resolution of 2 cm<sup>-1</sup> by accumulating 32 scans. The temperature was controlled by a Pike temperature controller and the gas composition was governed by mass flow control (MFC). The catalyst was pretreated at 500 °C for 1 h under flowing 20 vol% O<sub>2</sub> + N<sub>2</sub> (40 mL min<sup>-1</sup>) and was then cooled down to 100 °C. The background spectrum was recorded under flowing N<sub>2</sub> at 100 °C, which was further subtracted from the sample spectrum.

## 3 Results and discussion

### 3.1 Catalytic performance

Fig. 1 shows the NH<sub>3</sub>-SCR catalytic performance of the MnO<sub>x</sub>/TiO<sub>2</sub>(*n*) catalysts with various TiO<sub>2</sub> particle sizes. For all the catalysts, NO<sub>x</sub> conversion firstly increased gradually from 65 °C

to 265–290 °C, and then decreased steadily with further increasing of the temperature to 400 °C. The maximum NO<sub>x</sub> conversion temperature was 265 °C for MnO<sub>x</sub>/TiO<sub>2</sub>(5–10), MnO<sub>x</sub>/TiO<sub>2</sub>(10–25) and MnO<sub>x</sub>/TiO<sub>2</sub>(40) and 290 °C for MnO<sub>x</sub>/TiO<sub>2</sub>(60). These results can be attributed to various SCR reaction pathways based on the NO<sub>2</sub>/NO ratio.<sup>6,7,9,10,32</sup> The pathway of the NH<sub>3</sub>-SCR reaction was regarded to occur *via* three reaction routes; namely, standard-, fast- and slow-SCR, which rest on the NO<sub>2</sub>/NO fraction in the reaction feed.<sup>7</sup>



As shown in Fig. 1, at the initial stage, the reaction occurred through a standard route. With increasing reaction temperature, the NO<sub>2</sub>/NO ratio increased through NO oxidation, inducing a variation in the main reaction pathway from the standard route to fast SCR. With increasing the reaction temperature, the ratio of NO<sub>2</sub>/NO increased above 1, causing the main reaction pathway to change to slow SCR from fast SCR.<sup>33,34</sup> By further increasing reaction temperature, the NO<sub>2</sub>/NO ratio decreased with the restriction of the thermal equilibrium of NO<sub>2</sub> decomposition. The main reaction pathway changed to the standard SCR, thus decreasing the SCR catalytic activity.<sup>33</sup>

In order to compare the catalytic performance of the various catalysts, T50 and T80 (the temperatures of NO<sub>x</sub> conversion at 50% and 80%) were introduced and are shown in Fig. 1B. T50 decreased from 160 °C to 155 °C and 135 °C, when the TiO<sub>2</sub> particle sizes decreased from 60 nm to 40 nm and 10–25 nm. Nevertheless, by further decreasing the TiO<sub>2</sub> particle size from 10–25 nm to 5–10 nm, T50 increased from 135 °C to 185 °C. A similar trend could be found in T80 as T50 over the corresponding catalysts. The catalytic activity of the MnO<sub>x</sub>/TiO<sub>2</sub>(*n*) catalysts showed a volcano-type dependence on the TiO<sub>2</sub> particle size, reaching a maximum at 10–25 nm. These results illustrated that the SCR performance of the MnO<sub>x</sub>/TiO<sub>2</sub>(*n*) catalysts varied with the TiO<sub>2</sub> support particle size. Soykal *et al.*<sup>30</sup> reported that the support particle size could change the reducibility and relative amount of redox sites on the catalyst surface. Generally, the SCR activity could be dependent on the surface acidity property, redox property and their synergistic effects.<sup>6,32</sup> The various initial TiO<sub>2</sub> support sizes could affect the characteristics of the manganese oxide active sites, and could thereby have an impact on the SCR catalytic performance. Therefore, the characteristics of the supported manganese catalysts, such as redox, acidity and their synergistic effects, were then investigated to assess the effect of initial TiO<sub>2</sub> support particle size on the SCR performance of the MnO<sub>x</sub>/TiO<sub>2</sub>(*n*) catalysts.

### 3.2 TEM

Fig. 2 shows TEM images of various TiO<sub>2</sub> support sizes. The size distribution of the various TiO<sub>2</sub> supports was 8.2  $\pm$  3.5 nm, 18.3  $\pm$  7.4 nm, 43.5  $\pm$  5.2 nm and 63.6  $\pm$  5.2 nm, similar to as purchased. However, the size distributions of the various MnO<sub>x</sub>/



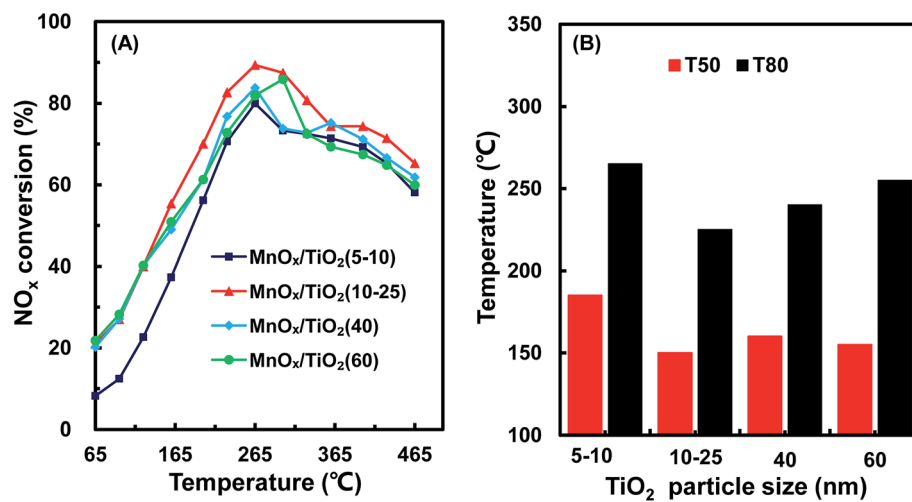


Fig. 1 NO<sub>x</sub> conversion (A), T50 and T80 (B) of MnO<sub>x</sub>/TiO<sub>2</sub>(*n*) with various TiO<sub>2</sub> particle sizes.

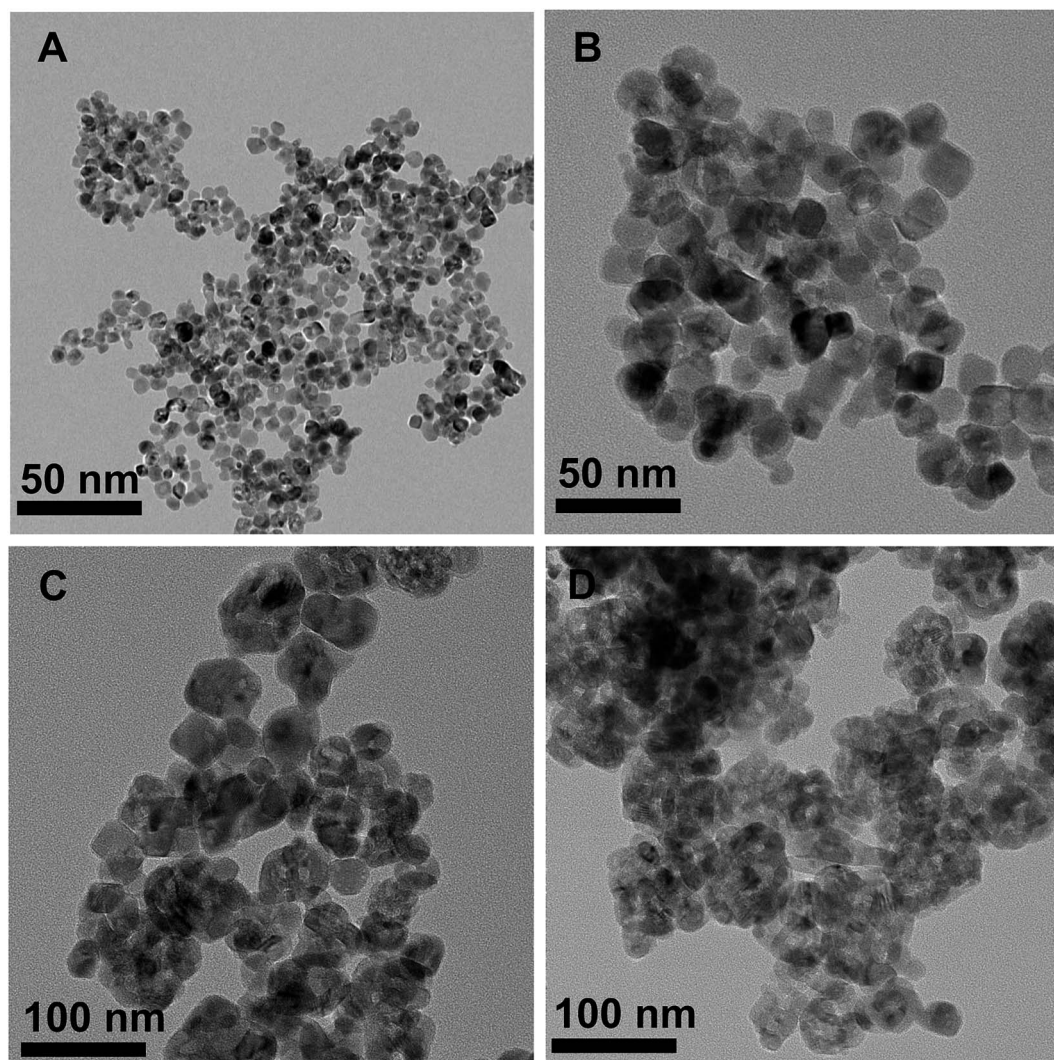


Fig. 2 TEM images of the various TiO<sub>2</sub>(*n*) supports of *n* = 5–10 (A), 10–25 (B), 40 (C) and 60 (D).



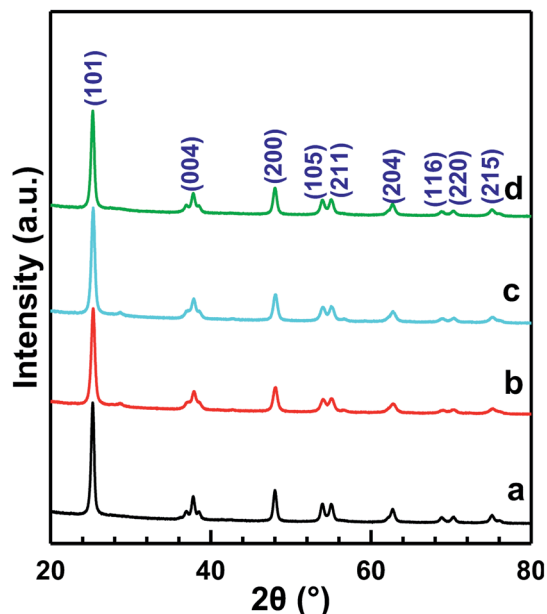


Fig. 3 XRD patterns of  $\text{MnO}_x/\text{TiO}_2(n)$  catalysts:  $n = 5-10$  (a),  $10-25$  (b),  $40$  (c) and  $60$  (d).

$\text{TiO}_2$  catalysts, as shown in Fig. S1,<sup>†</sup> were similar. All the  $\text{MnO}_x/\text{TiO}_2$  catalysts had an average diameter of *ca.* 55 nm. These results revealed that the impregnation and calcination process resulted in the variation in the particle sizes of the  $\text{MnO}_x/\text{TiO}_2$  catalysts.

### 3.3 XRD

Fig. 3 shows the XRD patterns of  $\text{MnO}_x/\text{TiO}_2(n)$  with various  $\text{TiO}_2$  particle sizes. All of the catalysts showed the same  $2\theta$  diffraction positions and different diffraction intensities. The diffraction of  $2\theta$  at  $25.3^\circ$ ,  $37.8^\circ$ ,  $48.0^\circ$ ,  $53.9^\circ$ ,  $55.1^\circ$ ,  $62.8^\circ$ ,  $68.9^\circ$ ,  $70.5^\circ$  and  $75.2^\circ$  could be assigned to (101), (004), (200), (105), (211), (204), (116), (220) and (215) planes of anatase- $\text{TiO}_2$

(JCPDS, 65-5714), respectively. The theoretical monolayer coverage amount could be estimated from structural calculations.<sup>35-37</sup> Based on the cation density of  $\text{MnO}_x$ , a reference value of  $15 \text{ \AA}^2$  per  $\text{MnO}_x$  unit was used to calculate the monolayer surface coverage.<sup>35-37</sup> The virtual loading was *ca.* 3.1 wt% Mn for monolayer surface coverage, according to the surface area of our investigated samples. Mn loading in our investigated catalysts was 10 wt%, which was more than three times that of the monolayer manganese amount. However, no independent diffraction peaks corresponding to manganese oxides could be observed in all the samples, indicating that the incorporated manganese oxides were in a highly dispersed state or in an amorphous or poorly crystalline state. These results could be ascribed to the strong interaction between Mn and anatase  $\text{TiO}_2$ , which is in agreement with the previous reports.<sup>20,23</sup>

### 3.4 Textural properties of the catalysts

Fig. 4 shows the  $\text{N}_2$  adsorption/desorption isotherms and pore size distributions of the  $\text{MnO}_x/\text{TiO}_2(n)$  catalysts with various  $\text{TiO}_2$  particle sizes. For all the  $\text{MnO}_x/\text{TiO}_2(n)$  catalysts, the  $\text{N}_2$  adsorption/desorption isotherms show similar type IV behavior and hysteresis loops attributed to type H1. The corresponding quantification parameters of the textural properties, including BET specific surface area, total pore volume and average pore diameter, are shown in Table 1. All of the catalysts showed similar specific surface areas ( $50.2-57.4 \text{ m}^2 \text{ g}^{-1}$ ), pore volumes ( $0.27-0.29 \text{ mL g}^{-1}$ ) and mean pore diameters (20–27 nm). It should be noted that the pore sizes were much larger than the dynamic size of the feed gas, indicating that the pore structures of the  $\text{MnO}_x/\text{TiO}_2(n)$  catalysts were feasible for reactant molecule diffusion.

### 3.5 $\text{H}_2$ -TPR

The redox properties of catalysts play an important role in the  $\text{NH}_3$ -SCR reaction. Thus,  $\text{H}_2$ -TPR experiments were carried out

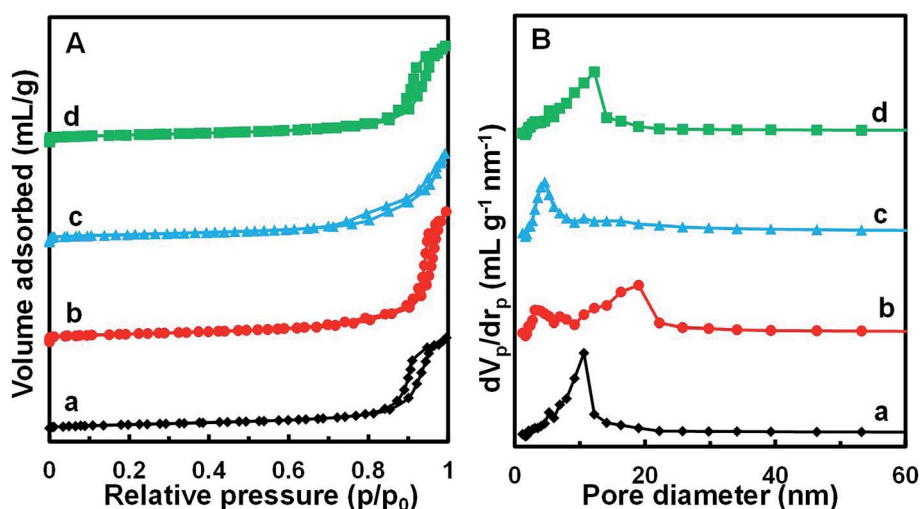


Fig. 4  $\text{N}_2$  adsorption/desorption isotherms (A) and BJH pore distribution curves (B) of  $\text{MnO}_x/\text{TiO}_2(n)$  catalysts:  $n = 5-10$  (a),  $10-25$  (b),  $40$  (c) and  $60$  (d).



**Table 1** BET specific surface area, total pore volume, mean pore diameter surface composition of  $\text{MnO}_x/\text{TiO}_2(n)$  catalysts with various  $\text{TiO}_2$  support particle sizes

Catalyst	BET surface area ( $\text{m}^2 \text{g}^{-1}$ )	Pore volume ( $\text{mL g}^{-1}$ )	Average pore diameter (nm)	$\text{Mn}^{4+}/\text{Mn}_{\text{total}}^a$
$\text{MnO}_x/\text{TiO}_2(5-10)$	51.5	0.29	22.2	0.29
$\text{MnO}_x/\text{TiO}_2(10-25)$	57.4	0.29	27.2	0.48
$\text{MnO}_x/\text{TiO}_2(40)$	54.0	0.27	19.8	0.35
$\text{MnO}_x/\text{TiO}_2(60)$	50.2	0.29	23.4	0.34

<sup>a</sup> Determined by XPS.

to determine the oxidative properties of the  $\text{MnO}_x/\text{TiO}_2(n)$  catalysts and the results are shown in Fig. 5. All of the catalysts exhibited two broad hydrogen consumption peaks. The lower temperature reduction peak in the temperature range of 300–450 °C could be attributed to the reduction of  $\text{Mn}^{4+}$  to  $\text{Mn}^{3+}$  and  $\text{Ti}^{4+}$  to  $\text{Ti}^{3+}$ , which originated from interaction between  $\text{MnO}_x$  and  $\text{TiO}_2$ .<sup>23,38–41</sup> The higher temperature peak in the temperature range of 450–600 °C could be ascribed to the reduction of  $\text{Mn}^{3+}$  to  $\text{Mn}^{2+}$ .<sup>38,42,43</sup> It should be noted that the temperature peaks were different for  $\text{MnO}_x/\text{TiO}_2(n)$  with different initial  $\text{TiO}_2$  particle sizes. For  $\text{MnO}_x/\text{TiO}_2(5-10)$ ,  $\text{MnO}_x/\text{TiO}_2(10-25)$ ,  $\text{MnO}_x/\text{TiO}_2(40)$  and  $\text{MnO}_x/\text{TiO}_2(60)$ , the reduction peaks at lower temperature were centered at 400 °C, 364 °C, 384 °C and 367 °C, while the higher temperature reduction peaks were 525 °C, 516 °C, 527 °C and 521 °C, respectively. In previous studies, the SCR performance of  $\text{MnO}_x/\text{TiO}_2$  catalysts has been related to the oxidation state of surface Mn atoms, especially the properties of surface  $\text{Mn}^{4+}$  species.<sup>38,42,43</sup> The lower peak temperature of  $\text{MnO}_x/\text{TiO}_2(n)$  represents a higher oxidative property and oxygen mobility. The order of the peak temperatures in the temperature

range of 300–450 °C for the  $\text{MnO}_x/\text{TiO}_2(n)$  catalysts was as follows:  $\text{MnO}_x/\text{TiO}_2(10-25)$  (364 °C) <  $\text{MnO}_x/\text{TiO}_2(60)$  (367 °C) <  $\text{MnO}_x/\text{TiO}_2(40)$  (384 °C) <  $\text{MnO}_x/\text{TiO}_2(5-10)$  (400 °C).  $\text{MnO}_x/\text{TiO}_2(60)$  and  $\text{MnO}_x/\text{TiO}_2(40)$  showed different trends in their corresponding SCR catalytic activity. The catalytic activity was not only decided by the properties of active sites, but also relied on the number of active sites. The peak area in the temperature range of 300–450 °C for  $\text{MnO}_x/\text{TiO}_2(40)$ , which was associated with the amount of  $\text{Mn}^{4+}$ , was higher than that for  $\text{MnO}_x/\text{TiO}_2(60)$ . Therefore, the properties and amount of  $\text{Mn}^{4+}$  in  $\text{MnO}_x/\text{TiO}_2(n)$  could also be affected by the  $\text{TiO}_2$  particle size, thus influencing the SCR catalytic activity.

### 3.6 $\text{O}_2$ -TPD

In order to further confirm the oxidative properties and oxygen mobility,  $\text{O}_2$ -TPD was then used to characterize the oxygen mobility of the  $\text{MnO}_x/\text{TiO}_2(n)$  catalysts. Fig. 6 shows the  $\text{O}_2$ -TPD curves of the  $\text{MnO}_x/\text{TiO}_2(n)$  catalysts with various  $\text{TiO}_2$  particle sizes. For all of the  $\text{MnO}_x/\text{TiO}_2(n)$  catalysts, there are two desorption peaks centered at 500–700 °C and 700–800 °C, respectively. The desorption of  $\text{O}_2$  at a temperature above 200 °C in  $\text{O}_2$ -TPD for the manganese-based catalysts is associated with the evolution of oxygen from the lattice (surface or bulk).<sup>44</sup> The lower temperature peak in the temperature range of 500–700 °C was attributed to the surface lattice oxygen and related to the surface oxygen vacancies, which is often correlated with a high oxidation ability.<sup>45,46</sup> The higher temperature peak at temperatures above 700 °C could be assigned to bulk lattice oxygen, which was generally not correlated to oxidation ability and strongly bound to the lattice.<sup>46</sup> The peak temperature in the temperature range of 500–700 °C for  $\text{MnO}_x/\text{TiO}_2(10-25)$  was 560 °C, which was lower than that of  $\text{MnO}_x/\text{TiO}_2(5-10)$  (630 °C),  $\text{MnO}_x/\text{TiO}_2(40)$  (621 °C) and  $\text{MnO}_x/\text{TiO}_2(60)$  (586 °C). Meanwhile, the order of the lower temperature peak amount was similar to  $\text{H}_2$ -TPR.

### 3.7 $\text{NH}_3$ -TPD

The surface acid sites of the catalysts played a significant role in the  $\text{NH}_3$ -SCR reaction, which could adsorb and activate  $\text{NH}_3$ .  $\text{NH}_3$ -TPD was used to study the surface acidity of  $\text{MnO}_x/\text{TiO}_2(n)$ , as depicted in Fig. 7. For all the  $\text{MnO}_x/\text{TiO}_2(n)$  catalysts, the  $\text{NH}_3$ -TPD curves featured a broad peak between 100 and 400 °C. All these desorption peaks were divided into two or three peaks based on the Gaussian peak shape model. The desorption peaks

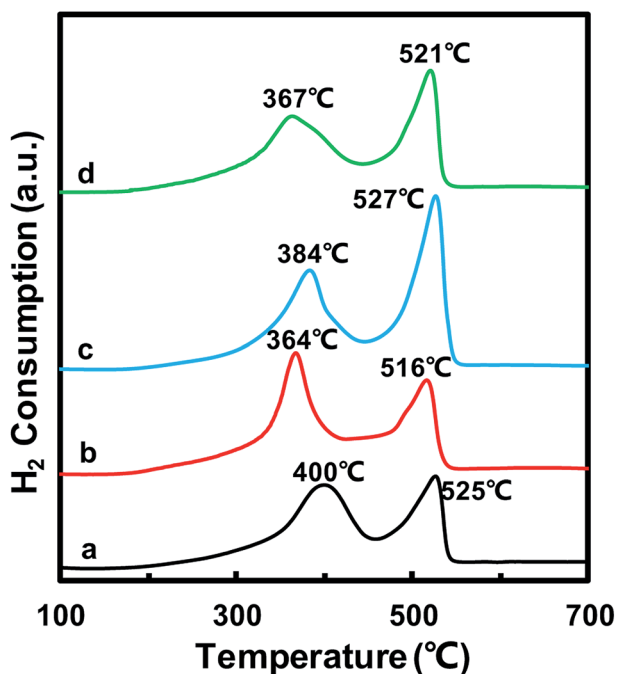


**Fig. 5**  $\text{H}_2$ -TPR profiles of the  $\text{MnO}_x/\text{TiO}_2(n)$  catalysts:  $n = 5-10$  (a),  $10-25$  (b),  $40$  (c) and  $60$  (d).



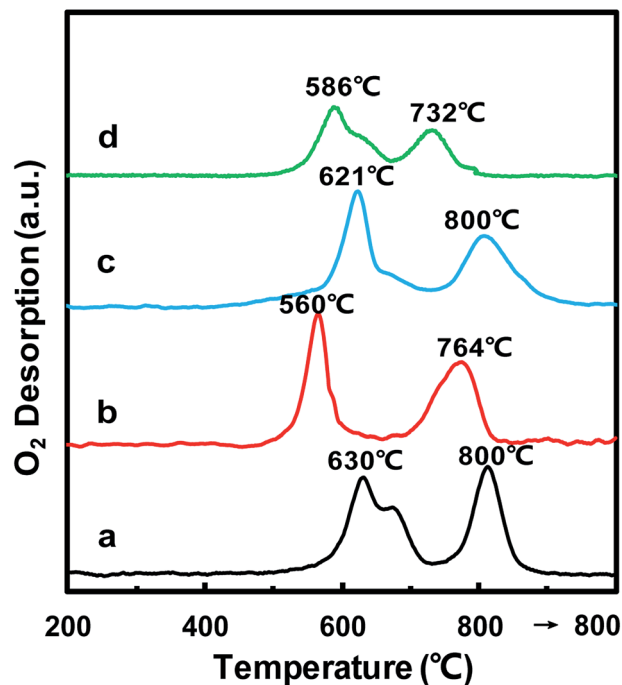


Fig. 6 O<sub>2</sub>-TPD profiles of MnO<sub>x</sub>/TiO<sub>2</sub>(*n*) catalysts of *n* = 5–10 (a), 10–25 (b), 40 (c) and 60 (d).

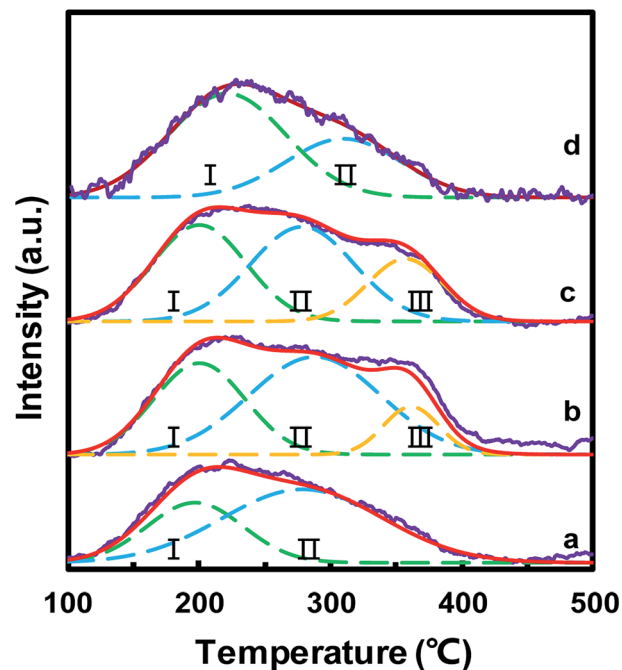


Fig. 7 NH<sub>3</sub>-TPD profiles of the MnO<sub>x</sub>/TiO<sub>2</sub>(*n*) catalysts: *n* = 5–10 (a), 10–25 (b), 40 (c) and 60 (d).

were labeled as I, II and III, according to the peak temperature from low to high, which could be attributed to the NH<sub>3</sub> desorbed from weak acid sites, medium acid sites and strong acid sites, respectively.<sup>17,47</sup> The peak temperature and corresponding area in NH<sub>3</sub>-TPD were calculated and are listed in Table 2. The peak temperature of MnO<sub>x</sub>/TiO<sub>2</sub> with TiO<sub>2</sub> < 40 nm was *ca.*

Table 2 Quantitative analysis of NH<sub>3</sub>-TPD for the MnO<sub>x</sub>/TiO<sub>2</sub>(*n*) catalysts

Catalyst	Temperature (°C)			Acid amount (μmol g <sup>-1</sup> )			
	T <sub>I</sub>	T <sub>II</sub>	T <sub>III</sub>	S <sub>I</sub>	S <sub>II</sub>	S <sub>III</sub>	S <sub>I</sub> + S <sub>II</sub> + S <sub>III</sub>
Mn/TiO <sub>2</sub> (5–10)	197	279	—	194	397	—	591
Mn/TiO <sub>2</sub> (10–25)	200	288	361	279	430	89	798
Mn/TiO <sub>2</sub> (40)	200	279	357	301	329	158	789
Mn/TiO <sub>2</sub> (60)	222	310	—	408	228	—	636

200 °C, which is lower than that of MnO<sub>x</sub>/TiO<sub>2</sub>(60). More importantly, the order of the acid amount for the MnO<sub>x</sub>/TiO<sub>2</sub>(*n*) catalysts was as follows: MnO<sub>x</sub>/TiO<sub>2</sub>(10–25) > MnO<sub>x</sub>/TiO<sub>2</sub>(40) > MnO<sub>x</sub>/TiO<sub>2</sub>(60) > MnO<sub>x</sub>/TiO<sub>2</sub>(5–10), which is also in accordance with the catalytic activity of the counterpart catalysts, suggesting that the particle size of the support not only influences the oxidizing ability but also the acidic properties.

Compared with larger TiO<sub>2</sub> support particle size, a smaller TiO<sub>2</sub> particle size could provide a greater boundary area between active sites and supports, which is beneficial for the synergistic effect between acid sites and redox sites. As previously reported, low-temperature selective catalytic reduction mainly occurs *via* a Langmuir–Hinshelwood mechanism. The SCR activity was controlled not only by the activation of NO, O<sub>2</sub> and NH<sub>3</sub> reactant, but also by the synergistic effect between acid sites and redox sites.

### 3.8 XPS

In order to further acquire information regarding the oxidation state of manganese on the catalyst surface, XPS spectra of the MnO<sub>x</sub>/TiO<sub>2</sub>(*n*) catalysts were recorded. Fig. 8 shows the Mn 2p spectra of the MnO<sub>x</sub>/TiO<sub>2</sub> catalysts with various TiO<sub>2</sub> particle sizes. The Mn 2p spectra of MnO<sub>x</sub>/TiO<sub>2</sub>(*n*) catalysts were deconvoluted based on the Gaussian–Lorentzian (GL(30)) line shape after subtracting a Shirley baseline. All the Mn 2p<sub>1/2</sub> and 2p<sub>3/2</sub> peaks of each Mn species have the same half height peak width and the center of the Mn 2p<sub>1/2</sub> and 2p<sub>3/2</sub> peaks was 11.7 eV. Mn 2p spectra of the MnO<sub>x</sub>/TiO<sub>2</sub>(*n*) catalysts could be divided into two peaks with maxima at 644.1–645.3 eV and 641.9–642.5 eV, which can be assigned to Mn<sup>4+</sup> and Mn<sup>3+</sup>, respectively.<sup>23,41,42,48,49</sup> The quantitation results of the Mn<sup>4+</sup>/Mn molar ratio in XPS spectra are shown in Table 1. It can be seen that the Mn<sup>4+</sup>/Mn molar ratio of the MnO<sub>x</sub>/TiO<sub>2</sub>(10–25) catalyst was 0.48, which is higher than 0.35 for MnO<sub>x</sub>/TiO<sub>2</sub>(40), 0.34 for MnO<sub>x</sub>/TiO<sub>2</sub>(60) and 0.29 for MnO<sub>x</sub>/TiO<sub>2</sub>(5–10). Moreover, the order of the surface Mn<sup>4+</sup>/Mn molar ratio on the MnO<sub>x</sub>/TiO<sub>2</sub>(*n*) catalysts was as follows: MnO<sub>x</sub>/TiO<sub>2</sub>(10–25) > MnO<sub>x</sub>/TiO<sub>2</sub>(40) > MnO<sub>x</sub>/TiO<sub>2</sub>(60) > MnO<sub>x</sub>/TiO<sub>2</sub>(5–10), which agrees well with the SCR catalytic performance. These results demonstrate that the TiO<sub>2</sub> particle size could influence the oxidation state of surface manganese oxides, leading to the variation in Mn<sup>4+</sup> concentration, which could be ascribed to the interaction between manganese oxides and titanium.<sup>42,50</sup> Thirupathi *et al.* also investigated the effect of the surface manganese species on the SCR performance and found that surface Mn<sup>4+</sup> on the TiO<sub>2</sub>



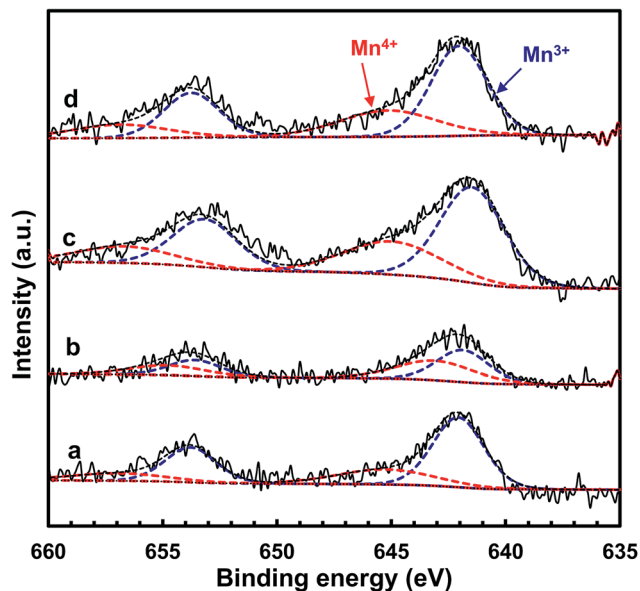


Fig. 8 XPS spectra for Mn 2p of the  $\text{MnO}_x/\text{TiO}_2(n)$  catalysts:  $n = 5-10$  (a), 10–25 (b), 40 (c) and 60 (d).

support was directly associated with the SCR performance.<sup>42</sup> All of these results revealed that initial  $\text{TiO}_2$  particle size can affect the oxidizing ability and oxygen mobility. The higher oxidizing ability could increase the  $\text{NO}_2/\text{NO}_x$  ratio in the actual reaction feed, which could increase the proportion of “fast SCR” reaction route, and thereby enhance the SCR activity.<sup>50</sup>

### 3.9 In situ DRIFTS studies

**3.9.1 NO + O<sub>2</sub> adsorption.** In order to understand the mechanism of the  $\text{MnO}_x/\text{TiO}_2(n)$  catalysts, DRIFT spectra of  $\text{NO} + \text{O}_2$  adsorption over  $\text{MnO}_x/\text{TiO}_2(10-25)$  were studied. Fig. 9 shows the DRIFT spectra of  $\text{NO} + \text{O}_2$  adsorption over  $\text{MnO}_x/\text{TiO}_2(10-25)$  for various times at 100 °C. Bands at 1607, 1580, 1492, 1446, 1300, 1282 and 1257  $\text{cm}^{-1}$  were detected. The band at 1607  $\text{cm}^{-1}$  could be ascribed to the bridge nitrate.<sup>50–53</sup> The bands at 1580, 1300 and 1282  $\text{cm}^{-1}$  could be assigned to bidentate nitrate.<sup>41,51–54</sup> The bands at 1492 and 1257  $\text{cm}^{-1}$  could be identified as monodentate nitrate.<sup>52,55</sup> The wide peak in the region of 1430–1550  $\text{cm}^{-1}$  could be attributed to the bidentate nitrate on the surface of the sample.<sup>52,55</sup> The band at 1446  $\text{cm}^{-1}$  was assigned to nitro compounds.<sup>54</sup> In the first 5 min, only bridge nitrate (band at 1607  $\text{cm}^{-1}$ ) and bidentate nitrate (bands at 1580, 1300 and 1282  $\text{cm}^{-1}$ ) were detected on the manganese oxides. With increasing time, monodentate nitrate (bands at 1492 and 1257  $\text{cm}^{-1}$ ) on the manganese oxides appeared. Meanwhile, bidentate nitrate on the surface of the sample (the wide peak in the region of 1430–1550  $\text{cm}^{-1}$ ) increased with exposure time. These results illustrated that  $\text{NO}_x$  first adsorbed on manganese oxides as bridge and bidentate nitrate, and then as monodentate nitrate.

**3.9.2 NH<sub>3</sub> adsorption after NO + O<sub>2</sub> adsorption.** To understand the role of various adsorbed  $\text{NO}_x$  species during the  $\text{NH}_3$ -SCR reaction, the *in situ* DRIFT spectra for the pre-adsorbed  $\text{NO} + \text{O}_2$  and  $\text{NH}_3$  at 100 °C as a function of time

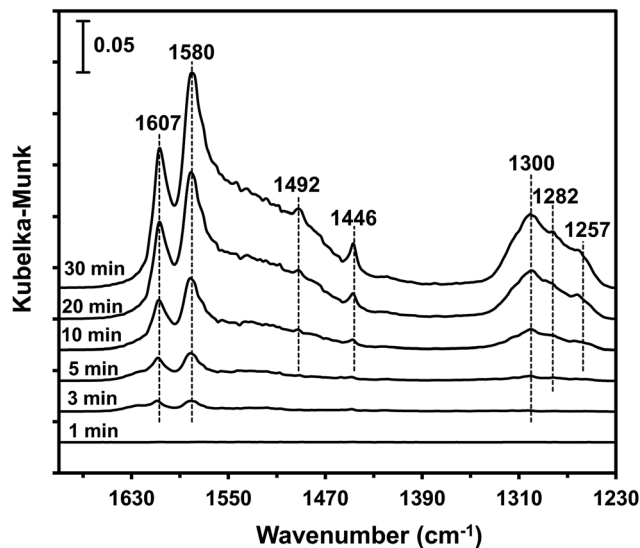


Fig. 9 DRIFT spectra of  $\text{MnO}_x/\text{TiO}_2(10-25)$  exposed to 500 ppm  $\text{NO} + 5\% \text{O}_2 + \text{N}_2$  at 100 °C for various times.

are shown in Fig. 10. A reaction temperature of 100 °C was chosen to decrease the reaction rate; therefore the surface species on the catalyst surface could be enhanced to a detectable level.<sup>56</sup> When 500 ppm  $\text{NH}_3$  was introduced to the catalyst pretreated by  $\text{NO} + \text{O}_2$ , the intensity of the band at 1607  $\text{cm}^{-1}$  assigned to bridge nitrate on manganese oxides decreased immediately with the increase of time. Meanwhile, the intensity of the bands at 1580 and 1295  $\text{cm}^{-1}$  (shown in Fig. 10C) assigned to bidentate nitrate on the manganese oxides decreased gradually. However, the variation of the intensity of the band at 1257  $\text{cm}^{-1}$  assigned to monodentate nitrate on the manganese oxides was different, and remained constant, indicating that the monodentate nitrate was not contributing to the SCR reaction at 100 °C. Simultaneously, the intensity of the bands at 3341 and 3244  $\text{cm}^{-1}$  (shown in Fig. 10D) assigned to asymmetric stretching and symmetric stretching of  $\text{NH}_3$  coordinated to Lewis acid sites, increased immediately with the addition of  $\text{NH}_3$ .<sup>51,57,58</sup> It is reasonable to assume that the band at 1598  $\text{cm}^{-1}$  assigned to coordinated  $\text{NH}_3$  on Lewis acid sites was caused by the overlap of the bridge and bidentate nitrates in the regions of 1630 and 1550  $\text{cm}^{-1}$ . These results indicated that bridge and bidentate nitrates were the main contributors to the low-temperature SCR reaction, fitting the Langmuir–Hinshelwood mechanism suggested in previous works.<sup>55,57,59,60</sup> It should be noted that the band due to the bridge and bidentate nitrates did not completely vanish, even when the  $\text{NH}_3$  purging time was prolonged to 60 min, suggesting that  $\text{NO}_x$  species adsorbed on various manganese species showed different SCR activity. More importantly, the band (shown in Fig. 10B) assigned to bridge nitrate shifted from 1607  $\text{cm}^{-1}$  to 1600  $\text{cm}^{-1}$ , illustrating that adsorbed  $\text{NO}_x$  species at higher wavenumbers in the IR band showed superior SCR activity, since the IR band position was statistically evaluated according to the similar structures of the various surface manganese species. Based on our previous characterization results, such as those from  $\text{H}_2$ -TPR,  $\text{O}_2$ -TPD and XPS, the surface valence states of manganese with various





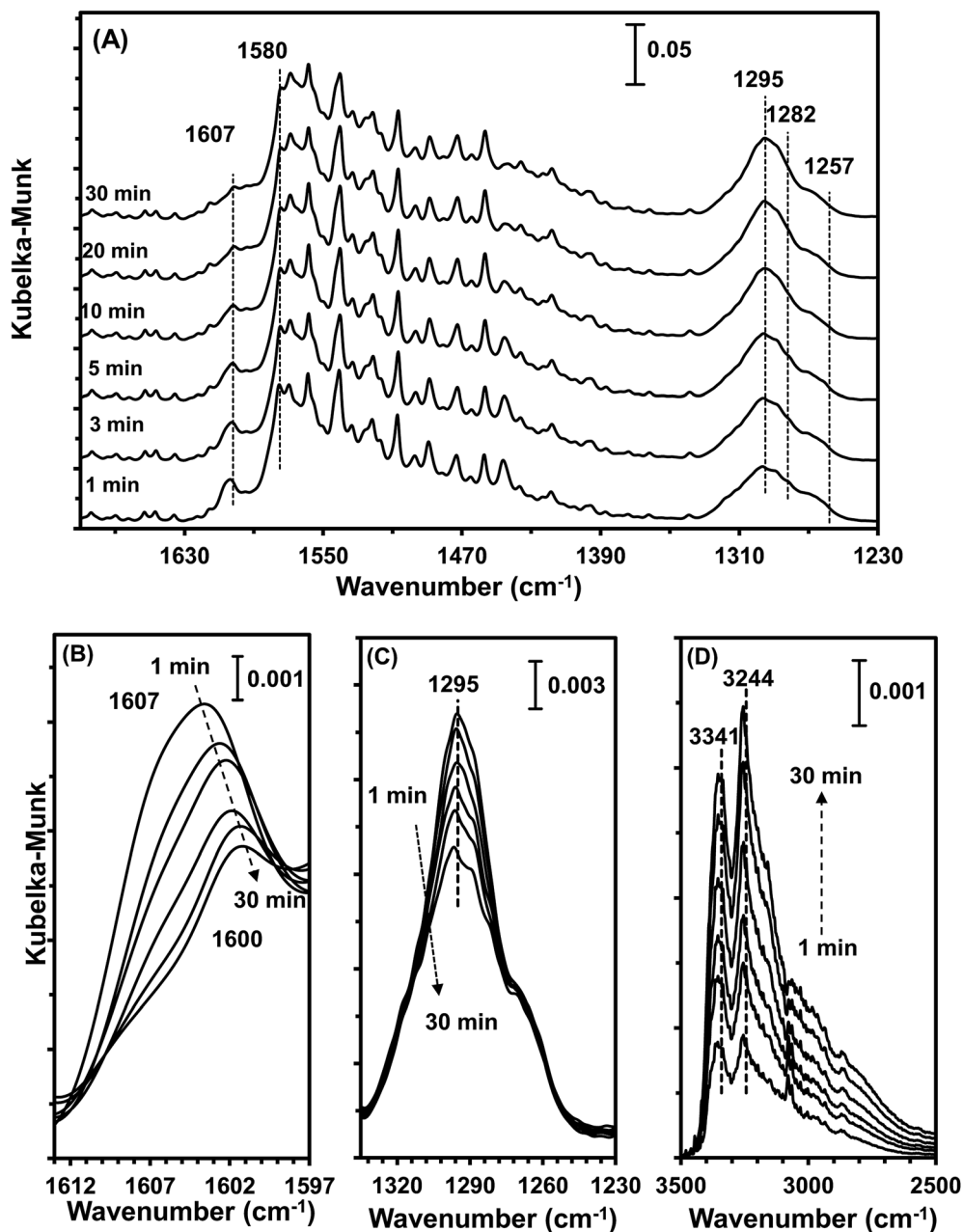


Fig. 10 DRIFT spectra of  $\text{MnO}_x/\text{TiO}_2(10-25)$  pretreated by exposure to 500 ppm  $\text{NO} + 5\% \text{O}_2 + \text{N}_2$  followed by exposure to 500 ppm  $\text{NH}_3 + \text{N}_2$  at  $100^\circ\text{C}$  for various times.

initial support sizes contained different compositions of  $\text{Mn}^{4+}$  and  $\text{Mn}^{3+}$ . The IR vibration frequencies in the N–O stretching modes could be varied *via* the formation of  $\pi$ -back bands.<sup>61</sup> With high-valent cations ( $\text{Mn}^{4+}$ ), which are poor in d-electrons, the extent of  $\pi$ -back donation is lower than that in low-valent cations ( $\text{Mn}^{3+}$ ), thus increasing the vibration frequency or wavenumber. The bridge nitrate at a higher wavenumber could be attributed to the  $\text{NO}_x$  adsorbed on the high-valent manganese species,  $\text{Mn}^{4+}$ . Based on the previous DRIFTS results, the higher wavenumber IR band ( $1607\text{ cm}^{-1}$ ) decreased more quickly than the lower one. Therefore, we deduced that  $\text{NO}_x$

adsorbed species on  $\text{Mn}^{4+}$  was the dominant factor influencing the low-temperature SCR activity.

**3.9.3  $\text{NO} + \text{O}_2$  adsorption after  $\text{NH}_3$  adsorption.** Furthermore, in order to understand the function of adsorbed  $\text{NH}_3$  species during the  $\text{NH}_3$ -SCR reaction, DRIFT spectra of  $\text{MnO}_x/\text{TiO}_2(10-25)$  in a flow of  $\text{NO} + \text{O}_2$  were collected, after the catalyst was pre-exposed to a  $\text{NH}_3$  for 60 min followed by  $\text{N}_2$  purging for 30 min at  $100^\circ\text{C}$ , as shown in Fig. S2.† The intensity of the bands at 3410 and  $3244\text{ cm}^{-1}$  assigned to NH stretching remained unchanged, illustrating that the low-temperature SCR reaction did not occur *via* an Eley–Rideal mechanism but *via*



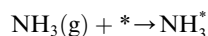
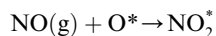
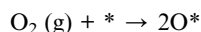
a Langmuir–Hinshelwood mechanism, which coincides with previous work.<sup>6</sup>

### 3.10 Origin of SCR activity

Combining the results obtained in this study, we could conclude that the low-temperature SCR activity over MnO<sub>x</sub>/TiO<sub>2</sub> occurred *via* a Langmuir–Hinshelwood mechanism.

Therefore, the NH<sub>3</sub>-SCR reaction over MnO<sub>x</sub>/TiO<sub>2</sub> can be described by the following pathways.

At low temperature, the reaction pathway occurred as a Langmuir–Hinshelwood mechanism.<sup>6</sup>



The type of adsorbed NO<sub>x</sub> species on manganese oxides has a prominent effect on the SCR activity. The order of SCR activity of various adsorbed nitrates was as follows: bridge nitrate > bidentate nitrate > monodentate nitrate. The bridge nitrate and bidentate nitrate were the main contributors to the SCR activity, while the monodentate nitrate showed no activity, which agreed with previous work.<sup>50</sup> Moreover, among all the bridge nitrates on various manganese oxides, bridge nitrate on the high-valence manganese species (*e.g.* Mn<sup>4+</sup>) was the most active species in the low-temperature SCR reaction, which could be proved by the blue shift on the DRIFT spectra in a flow of NH<sub>3</sub> after pretreatment with NO + O<sub>2</sub>. A higher Mn<sup>4+</sup>/Mn molar ratio could produce more bridge nitrate on Mn<sup>4+</sup>, thus increasing the SCR activity.

## 4 Conclusions

In this work, a series of MnO<sub>x</sub>/TiO<sub>2</sub> catalysts with various initial TiO<sub>2</sub> particle sizes was prepared *via* an impregnation method for the selective catalytic reduction of NO with NH<sub>3</sub>. The MnO<sub>x</sub>/TiO<sub>2</sub>(10–25) catalyst showed superior low-temperature SCR catalytic activity. The XRD results illustrated a high dispersion of manganese oxides on all the catalysts *via* interactions between manganese oxides and anatase TiO<sub>2</sub>. H<sub>2</sub>-TPR, O<sub>2</sub>-TPD, NH<sub>3</sub>-TPD and XPS results indicated that the acid amount and Mn<sup>4+</sup>/Mn molar ratio were dependent on the initial TiO<sub>2</sub> support particle size. The order of surface acidity and Mn<sup>4+</sup>/Mn molar ratio was as follows: MnO<sub>x</sub>/TiO<sub>2</sub>(10–25) > MnO<sub>x</sub>/TiO<sub>2</sub>(40) > MnO<sub>x</sub>/TiO<sub>2</sub>(60) > MnO<sub>x</sub>/TiO<sub>2</sub>(5–10), which agreed well with the order of SCR activity on the corresponding catalysts. Furthermore, the *in situ* DRIFTS results showed that the low-temperature SCR reaction occurred *via* a Langmuir–Hinshelwood mechanism and the adsorbed NO<sub>x</sub> was the key factor in

the low-temperature SCR activity. The order of adsorbed NO<sub>x</sub> species activity on manganese oxides was as follows: bridge nitrate > bidentate nitrate > monodentate nitrate. Moreover, the bridge nitrate on Mn<sup>4+</sup> was the greatest contributor to the low-temperature SCR activity. The variation of the initial TiO<sub>2</sub> support particle size influenced the surface Mn<sup>4+</sup>/Mn molar ratio of the MnO<sub>x</sub>/TiO<sub>2</sub> catalysts, which would promote the reactivity of the bridge nitrate, therefore enhancing SCR performance.

## Conflicts of interest

There are no conflicts to declare.

## Acknowledgements

We acknowledge the financial support from the China Postdoctoral Science Foundation (2017M613143), the Natural Science Foundation of Shaanxi Province of China (2017JQ2016), and the National Natural Science Foundation of China (21802107).

## References

- X. Liu, Y. Zhang, W. Han, A. Tang, J. Shen, Z. Cui, P. Vitousek, J. W. Erisman, K. Goulding, P. Christie, A. Fangmeier and F. Zhang, *Nature*, 2013, **494**, 459–462.
- Y. Cheng, G. Zheng, C. Wei, Q. Mu, B. Zheng, Z. Wang, M. Gao, Q. Zhang, K. He, G. Carmichael, U. Poschl and H. Su, *Sci. Adv.*, 2016, **2**, e160153012.
- S. Roy and A. Baiker, *Chem. Rev.*, 2009, **109**, 4054–4091.
- Z. Hu, K. Q. Sun, W. Z. Li and B.-Q. Xu, *Catal. Today*, 2010, **158**, 432–438.
- Z. Hu, W.-Z. Li, K.-Q. Sun and B.-Q. Xu, *Catal. Sci. Technol.*, 2013, **3**, 2062–2071.
- C. Liu, J. Shi, C. Gao and C. Niu, *Appl. Catal., A*, 2016, **522**, 54–69.
- R. Zhang, N. Liu, Z. Lei and B. Chen, *Chem. Rev.*, 2016, **116**, 3658–3721.
- J. Wang, H. Zhao, G. Haller and Y. Li, *Appl. Catal., B*, 2017, **202**, 346–354.
- W. Shan and H. Song, *Catal. Sci. Technol.*, 2015, **5**, 4280–4288.
- Z. Liu, J. Li and S. I. Woo, *Energy Environ. Sci.*, 2012, **5**, 8799–8814.
- F. Liu, W. Shan, D. Pan, T. Li and H. He, *Chin. J. Catal.*, 2014, **35**, 1438–1445.
- A. M. Beale, F. Gao, I. Lezcano-Gonzalez, C. H. F. Peden and J. Szanyi, *Chem. Soc. Rev.*, 2015, **44**, 7371–7405.
- X. Hu, L. Huang, J. Zhang, H. Li, K. Zha, L. Shi and D. Zhang, *J. Mater. Chem. A*, 2018, **6**, 2952–2963.
- K. Zha, L. Kang, C. Feng, L. Han, H. Li, T. Yan, P. Maitrad, L. Shi and D. Zhang, *Environ. Sci.: Nano*, 2018, **5**, 1408–1419.
- K. Zha, S. Cai, H. Hu, H. Li, T. Yan, L. Shi and D. Zhang, *J. Phys. Chem. C*, 2017, **121**, 25243–25254.
- C. Li, X. Tang, H. Yi, L. Wang, X. Cui, C. Chu, J. Li, R. Zhang and Q. Yu, *Appl. Surf. Sci.*, 2018, **428**, 924–932.



- 17 Z. Fan, J. Shi, C. Gao, G. Gao, B. Wang and C. Niu, *ACS Appl. Mater. Interfaces*, 2017, **9**, 16117–16127.
- 18 L. Yan, Y. Liu, K. Zha, H. Li, L. Shi and D. Zhang, *ACS Appl. Mater. Interfaces*, 2017, **9**, 2581–2593.
- 19 P. G. Smirniotis, D. A. Pena and B. S. Uphade, *Angew. Chem., Int. Ed.*, 2001, **40**, 2479–2482.
- 20 P. G. Smirniotis, P. M. Sreekanth, D. A. Peña and R. G. Jenkins, *Ind. Eng. Chem. Res.*, 2006, **45**, 6436–6443.
- 21 Y. J. Kim, H. J. Kwon, I. Nam, J. W. Choung, J. K. Kil, H. Kim, M. Cha and G. K. Yeo, *Catal. Today*, 2010, **151**, 244–250.
- 22 J. Li, J. Chen, R. Ke, C. Luo and J. Hao, *Catal. Commun.*, 2007, **8**, 1896–1900.
- 23 P. R. Ettireddy, N. Ettireddy, S. Mamedov, P. Boolchand and P. G. Smirniotis, *Appl. Catal., B*, 2007, **76**, 123–134.
- 24 S. Yang, F. Qi, S. Xiong, H. Dang, Y. Liao, P. K. Wong and J. Li, *Appl. Catal., B*, 2016, **181**, 570–580.
- 25 B. Xu, J. Wei, Y. Yu, J. Li and Q. Zhu, *Top. Catal.*, 2003, **22**, 77–85.
- 26 B. Xu, J. Wei, Y. Yu, Y. Li, J. Li and Q. Zhu, *J. Phys. Chem. B*, 2003, **107**, 5203–5207.
- 27 Q. Zhang, Y. Li and B. Xu, *Catal. Today*, 2004, **98**, 601–605.
- 28 M. M. Pakulska, C. M. Grgicak and J. B. Giorgi, *Appl. Catal., A*, 2007, **332**, 124–129.
- 29 M. Murdoch, G. I. N. Waterhouse, M. A. Nadeem, J. B. Metson, M. A. Keane, R. F. Howe, J. Llorca and H. Idriss, *Nat. Chem.*, 2011, **3**, 489–492.
- 30 I. I. Soykal, H. Sohn and U. S. Ozkan, *ACS Catal.*, 2012, **2**, 2335–2348.
- 31 Z. Hu, S. Tan, R. Mi, X. Li, D. Li and B. Yang, *Catal. Lett.*, 2018, **148**, 1490–1498.
- 32 J. Li, H. Chang, L. Ma, J. Hao and R. T. Yang, *Catal. Today*, 2011, **175**, 147–156.
- 33 M. Koebel, G. Madia and M. Elsener, *Catal. Today*, 2002, **73**, 239–247.
- 34 M. Devadas, O. Krocher, M. Elsener, A. Wokaun, N. Soger, M. Pfeifer, Y. Demel and L. Mussmann, *Appl. Catal., B*, 2006, **67**, 187–196.
- 35 E. F. Massoth, *Adv. Catal.*, 1978, **2**, 265–310.
- 36 G. C. Bond and S. F. Tahir, *Appl. Catal.*, 1991, **71**, 1–31.
- 37 J. M. Gallardo-Amores, T. Armaroli, G. Ramis, E. Finocchio and G. Busca, *Appl. Catal., B*, 1999, **22**, 249–259.
- 38 E. Park, S. Chin, J. Jeong and J. Jurng, *Microporous Mesoporous Mater.*, 2012, **163**, 96–101.
- 39 R. Guo, Q. Wang, W. Pan, W. Zhen, Q. Chen, H. Ding, N. Yang and C. Lu, *Appl. Surf. Sci.*, 2014, **317**, 111–116.
- 40 S. S. R. Putluru, L. Schill, A. D. Jensen, B. Siret, F. Tabaries and R. Fehrmann, *Appl. Catal., B*, 2015, **165**, 628–635.
- 41 W. Li, R. Guo, S. Wang, W. Pan, Q. Chen, M. Li, P. Sun and S. Liu, *Fuel Process. Technol.*, 2016, **154**, 235–242.
- 42 B. Thirupathi and P. G. Smirniotis, *J. Catal.*, 2012, **288**, 74–83.
- 43 S. M. Lee, K. H. Park, S. S. Kim, D. W. Kwon and S. C. Hong, *J. Air Waste Manage. Assoc.*, 2012, **62**, 1085–1092.
- 44 J. Luo, Q. Zhang, J. Garcia-Martinez and S. L. Suib, *J. Am. Chem. Soc.*, 2008, **130**, 3198–3207.
- 45 T. Seiyama, *Catal. Rev.*, 1992, **34**, 281–300.
- 46 M. Dhakad, S. S. Rayalu, R. Kumar, P. Doggali, S. Bakardjieva, J. Subrt, T. Mitsuhashi, H. Haneda and N. Labhsetwar, *Catal. Lett.*, 2008, **121**, 137–143.
- 47 S. Cimino, L. Lisi and M. Tortorelli, *Chem. Eng. J.*, 2016, **283**, 223–230.
- 48 Z. Wu, R. Jin, H. Wang and Y. Liu, *Catal. Commun.*, 2009, **10**, 935–939.
- 49 P. Sun, R. Guo, S. Liu, S. Wang, W. Pan and M. Li, *Appl. Catal., A*, 2017, **531**, 129–138.
- 50 H. Hu, K. Zha, H. Li, L. Shi and D. Zhang, *Appl. Surf. Sci.*, 2016, **387**, 921–928.
- 51 B. Jiang, Z. Li and S. Lee, *Chem. Eng. J.*, 2013, **225**, 52–58.
- 52 S. Wang, R. Guo, W. Pan, Q. Chen, P. Sun, M. Li and S. Liu, *Catal. Commun.*, 2017, **89**, 143–147.
- 53 L. Ma, Y. Cheng, G. Cavataio, R. W. McCabe, L. Fu and J. Li, *Appl. Catal., B*, 2014, **156–157**, 428–437.
- 54 Z. Wu, B. Jiang, Y. Liu, H. Wang and R. Jin, *Environ. Sci. Technol.*, 2007, **41**, 5812–5817.
- 55 L. Wei, S. Cui, H. Guo and L. Zhang, *Comput. Mater. Sci.*, 2018, **144**, 216–222.
- 56 M. Devadas, O. Kröcher, M. Elsener, A. Wokaun, G. Mitrikas, N. Söger, M. Pfeifer, Y. Demel and L. Mussmann, *Catal. Today*, 2007, **119**, 137–144.
- 57 F. Liu and H. He, *J. Phys. Chem. C*, 2010, **114**, 16929–16936.
- 58 L. Wei, S. Cui, H. Guo, X. Ma and L. Zhang, *J. Mol. Catal. A: Chem.*, 2016, **421**, 102–108.
- 59 E. Tronconi, I. Nova, C. Ciardelli, D. Chatterjee and M. Weibel, *J. Catal.*, 2007, **245**, 1–10.
- 60 H. Hu, S. Cai, H. Li, L. Huang, L. Shi and D. Zhang, *ACS Catal.*, 2015, **5**, 6069–6077.
- 61 H. I. Konstantin, *Catal. Rev.*, 2000, **42**, 71–144.

